

Threshold-independent method for single-shot readout of spin qubits in semiconductor quantum dots

Rui-Zi Hu,^{1,2} Sheng-Kai Zhu,^{1,2} Xin Zhang,^{1,2} Yuan Zhou,^{1,2} Ming Ni,^{1,2} Rong-Long Ma,^{1,2} Zhen-Zhen Kong,³ Gui-Lei Wang,^{3,4} Gang Cao,^{1,2} Hai-Ou Li,^{1,2,*} and Guo-Ping Guo^{1,2,5}

¹CAS Key Laboratory of Quantum Information, University of Science and Technology of China, Hefei, Anhui 230026, China

²CAS Center for Excellence and Synergetic Innovation Center in Quantum Information and Quantum Physics, University of Science and Technology of China, Hefei, Anhui 230026, China

³Key Laboratory of Microelectronics Devices & Integrated Technology, Institute of Microelectronics, Chinese Academy of Sciences, Beijing 100029, China

⁴Beijing Superstring Academy of Memory Technology, Beijing 100176, China

⁵Origin Quantum Computing Company Limited, Hefei, Anhui 230026, China

(Dated: June 9, 2022)

The single-shot readout data process is essential to access high-fidelity qubits for fault-tolerant quantum algorithms in semiconductor quantum dots. However, the visibility of the readout process is limited by the experimental hardwares and is sensitive to the choice of the thresholds. Here, we describe an alternative threshold-independent method for the single-shot readout of spin qubits in semiconductor quantum dots by demonstrating the linear dependence of the readout visibilities, dark counts, and measured spin state probabilities. We define an effective area to show the new technique is 60 times more efficient and robust. Also, the readout visibility for different readout times and threshold voltages reveals that these two parameters are not independent during the conventional optimizing process. Moreover, we discuss the influence of the electron temperature with a fixed external magnetic field and provide a preliminary demonstration for a single-shot readout up to 0.7 K/1.5 T in the future.

I. INTRODUCTION

Spin qubits in gate-defined silicon quantum dots (QDs) are promising to realize quantum computation for their long coherence time [1, 2], small footprint [3], potential scalability [4], and industrial manufacturability [5, 6]. In isotopically purified Si devices, the single-qubit gate fidelity has attained 99.9% [7, 8], and the two-qubit gate fidelity above 99% is reported [9–11]. Readout in single-spin qubits typically uses single-shot readout [12, 13], which utilizes the spin-state-dependent tunneling rate or quantum capacitance to measure the spin qubits with extra charge sensors or dispersive sensing techniques [14–16]. The spin states are distinguished by comparing the readout traces (x) with the threshold voltages (x_t) within the readout time (t_r). However, this process is sensitive to x_t and t_r , and will lower the overall fidelity of the gate operations.

To optimize the readout fidelity and visibility (V^R), several suggestions have been tried, e.g., wavelet edge detection [17], the analytical expression of the distribution [18, 19], statistic techniques [20–22], and the Monte-Carlo method [23]. Among these proposals, the Monte-Carlo method is now widely used to simulate the distributions of the experimental data numerically in Si-MOS QDs [24], Si/SiGe QDs [25], Ge QDs [26], single donors [27], and Nitrogen-Vacancy centers [28]. And a high fidelity readout in silicon single spin qubit has been achieved recently [29]. Even so, V^R is limited by the environment and experiment setup, e.g., the external magnetic field relative to the electron temperature (B_{ext}/T_e), relaxation time (T_1), tunneling rate ($\Gamma^{\text{in,out}}$), measurement

bandwidth, sample rate (Γ_s), and the filter frequency [30]. And the margin cost of improving the readout fidelity is not negligible [29].

Here, we describe a threshold-independent method for the single-shot readout of semiconductor spin qubits. By applying the rate equations [30–33] together with the Monte-Carlo method, we simulate the single-shot readout process and extract V^R as a function of t_r and x_t . We demonstrate that the measured probabilities of the excited spin state (P_{\uparrow}^M) are linear dependent on V^R from their definitions. Since the slope is the prepared probability of the excited spin state (P_{\uparrow}^I), robust to t_r and x_t , it supports us using P_{\uparrow}^I instead of P_{\uparrow}^M to realize a threshold-independent data processing method. Moreover, we use an effective area (A_{eff}) to show that the effectiveness of the threshold-independent method is about 60 times higher than the commonly used one, i.e., the threshold-dependent method. Finally, we discuss the influence of T_e with a fixed external magnetic field and provide a preliminary demonstration for a single-shot readout at 0.7 K/1.5 T in the future.

II. RESULT AND DISCUSSION

A. Single-shot readout

Fig. 1 outlines the processes of single-shot readout. The double quantum dots (DQD) in our experiment is similar to the device in Ref. [34]. (N_L , N_R) in the charge stability diagram in Fig. 1(a) represent the electrons occupied in the left and right QD. To measure the spin state of the first electron in the left QD, we deploy consecutive three-stage pulses, which consist of “Empty”, “Load & Wait” and “Readout” at the (0,0)-(1,0) transition line, illustrated by “E”, “W” and “R”

* haiouli@ustc.edu.cn

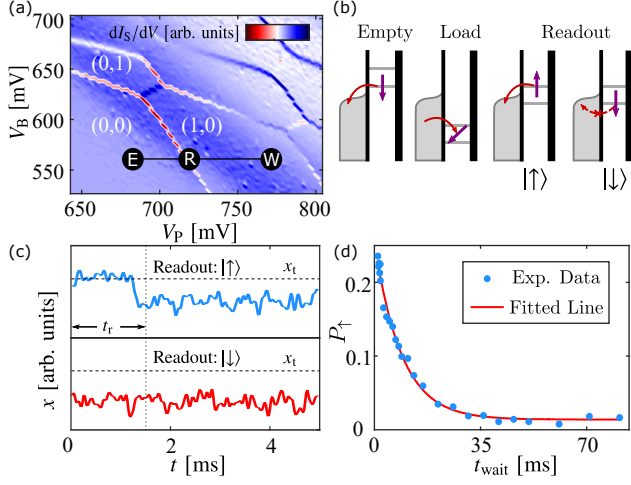


FIG. 1. (a) Charge stability diagram of the DQD measured by differentiating the single-electron transistor (SET) current (I_S) as a function of the V_B and V_P gate voltages. The pulse sequence for measuring the spin relaxation time (T_1) via the (0,0)-(1,0) charge transition line is overlaid on the data. (b) Illustration for the energy states of the pulse sequence: the measurement starts with emptying the electron in QD at point E, then injecting a random spin into it and waiting for a time at point W, finally moving to point R for STC conversion. (c) The readout traces (x) are achieved by amplifying I_S with a room temperature low noise current amplifier (DLCPA - 200) and a JFET preamplifier (SIM910), and then low-pass filtering the amplified signal using an analog filter (SIM965) with a bandwidth of 10 kHz. The blue and red curves represent spin up ($|\uparrow\rangle$) and spin down ($|\downarrow\rangle$) traces at point R, respectively. By comparing the maximum of the traces (x_{\max}) with the threshold voltage (x_t) within the readout time (t_r), we can distinguish the different spin states. (d) A typical exponential decay of spin-up probability with one thousand repeated measurements for each point. The exponential fitted value of $1/T_1$ is $112 \pm 6 \text{ s}^{-1}$.

in black circles in Fig. 1(a). Fig. 1(b) shows the corresponding energy states. Here we assume the excited spin state is $|\uparrow\rangle$. The location of the readout stage is carefully calibrated to ensure that the Fermi level of the reservoir is between the electrochemical potentials of spin-up and spin-down states.

The readout trace (x) is achieved by amplifying the single-electron transistor (SET) current (I_S) with a room temperature low noise current amplifier (DLCPA - 200) and a JFET preamplifier (SIM910), and then low-pass filtering the amplified signal using an analog filter (SIM965) with a bandwidth of 10 kHz.

The state-to-charge (STC) conversion is realized by distinguishing two different traces in the readout phase, as shown in Fig. 1(c). A single electron tunneling onto or off the QD causes a change in x . We distinguish the different spin states in QD by comparing x with x_t . If x remains below the threshold during the readout phase, we assume it is a $|\downarrow\rangle$ state and vice versa. Then we empty QD by raising the electrochemical potential and waiting for enough time. After the empty stage, we load a new electron with a random spin state and wait for the next readout stage.

We measure the electron spin relaxation time by repeating this three-stage pulse and changing the waiting time in the

loading stage. Fig. 1(d) shows an example of exponential decay of the measured spin-up probability $P_{\uparrow}^M = \rho \cdot e^{-t/T_1} + \alpha$, where ρ is the amplitude and α is the dark count. Additionally, we can manipulate the spin qubit by using a similar pulse and a microwave pulse, as reported in Ref. [35].

B. The readout visibility

We demonstrate a maximum $V^R = 85.4\%$ while measuring the spin relaxation time as shown in Fig. 2(a). $V^R = F_{\uparrow} + F_{\downarrow} - 1$ is calculated from the simulated data via Monte-Carlo method. F_{\downarrow} and F_{\uparrow} are the readout fidelities of $|\downarrow\rangle$ and $|\uparrow\rangle$. Fig. 2(b) illustrates the accuracy of the simulation with a high value of R squared (≈ 0.98). The insets in Fig 2.(b) show the fitting results of the averaged readout traces (\bar{x}) and the probability density function (PDF) of the traces maximum (x_{\max}) of the readout phase for every single measurement. The details about the simulation process are discussed in Appendix A, B & C [23, 27, 30–32].

To obtain a high V^R , state-to-charge conversion visibility (V^{STC}) and electrical detection visibility (V^E) need to be optimized. First, we apply the rate equations to \bar{x} , and obtain the tunneling rates of the state-to-charge conversion as shown in the left inset of Fig. 2(b): $\Gamma_{\uparrow}^{\text{out}} = 6.0 \pm 0.1 \text{ kHz}$, $\Gamma_{\downarrow}^{\text{out}} = 27 \pm 2 \text{ Hz}$ and $\Gamma_{\downarrow}^{\text{in}} = 1.39 \pm 0.04 \text{ kHz}$. Then, V^{STC} is obtained as a single peaked function of t_r as shown in Fig. 2(c). We describe the details of this part in Appendix B. For exceeding 99% V^{STC} , three criteria are given in Ref. [30], in-

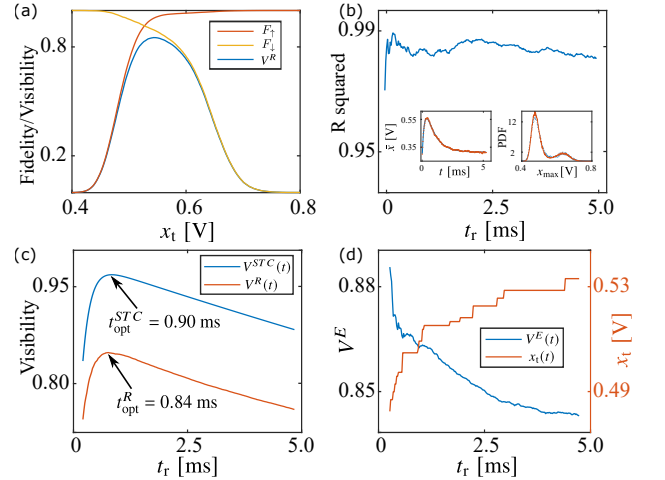


FIG. 2. (a) The fidelities of spin-up and spin-down state ($F_{\uparrow}, F_{\downarrow}$) and the related readout visibility (V^R) versus x_t . (b) The fitting model for the distribution of the experimental data has a high value of R squared (≈ 0.98), which indicates good accuracy of results. The insets show fitting results about the averaged traces (\bar{x}) and the probability density function (PDF) of the traces maximum (x_{\max}). (c) The state-to-charge (STC) conversion visibility (V^{STC}) versus the t_r and the corresponding maximum V^R . t_{opt}^R (the bottom arrow) and t_{opt}^{STC} (the top arrow) are not equal. (d) The electrical detection visibility (V^E) and the corresponding x_t as a function of t_r .

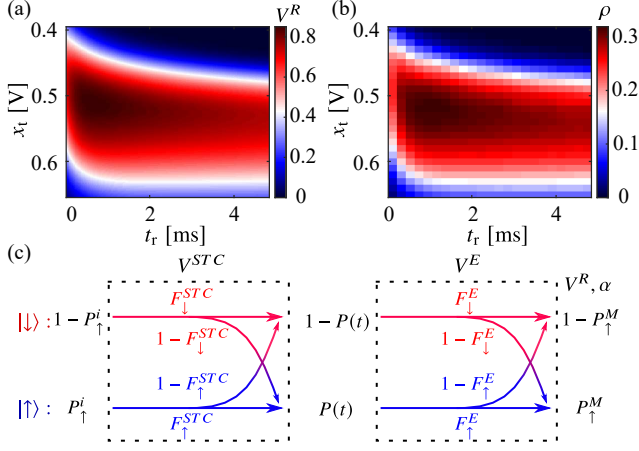


FIG. 3. (a)(b) V^R and the amplitude (ρ) as a function of t_r and x_t , which show a consistency in the image with scaled colors. (c) The qubits are prepared in $|\uparrow\rangle$ with P_{\uparrow}^I . Throughout the STC conversion (F_{\uparrow}^{STC} , F_{\downarrow}^{STC}), the electron tunnel out from QD with $P(t)$. Similarly, the electron are measured as $|\uparrow\rangle$ with P_{\uparrow}^M throughout the electrical detection (F_{\uparrow}^E , F_{\downarrow}^E).

cluding $E_z/T_e > 13$, $T_1 * \Gamma_{\uparrow}^{\text{out}} > 100$ and $\Gamma_s/\Gamma_{\downarrow}^{\text{in}} > 12$. Here, we have $\Gamma_s = 50$ kHz, $B_{\text{ext}} = 1.5$ T and $T_e = 180.5 \pm 8.1$ mK as mentioned in Ref. [34], thus the disagreement of the condition $E_z/T_e = 11.22 < 13$ limits that the maximum V^{STC} equals 97.15%.

To obtain V^E , we factorize V^R into $V^{STC} = F_{\uparrow}^{STC} + F_{\downarrow}^{STC} - 1$ and $V^E = F_{\uparrow}^E + F_{\downarrow}^E - 1$ as the following formula shows:

$$V^R = F_{\uparrow} + F_{\downarrow} - 1 = V^{STC} \times V^E. \quad (1)$$

Here, F_{\downarrow} , F_{\uparrow} is the following:

$$\begin{aligned} F_{\downarrow} &= F_{\downarrow}^{STC} F_{\downarrow}^E + (1 - F_{\downarrow}^{STC})(1 - F_{\uparrow}^E), \\ F_{\uparrow} &= F_{\uparrow}^{STC} F_{\uparrow}^E + (1 - F_{\uparrow}^{STC})(1 - F_{\downarrow}^E), \end{aligned} \quad (2)$$

For each t_r , we calculate V^R and V^{STC} first, and then have $V^E = V^R/V^{STC}$. Fig. 2(d) shows the maximum V^E and the corresponding optimum x_t as functions of t_r . Since the longer t_r we consider, the more noise is added to the trace, there is a clear trend that V^E decreases and x_t increases as t_r increases. The difference of the optimal t_r between V^E and V^{STC} reveals that t_r and x_t are not independent while optimizing V^R , and they should be considered simultaneously to get the maximum V^R instead of deemed in order.

C. Relation between P_{\uparrow}^M , P_{\uparrow}^I , and V^R

Now, we focus on the detail of V^R . First, we draw V^R as a t_r and x_t function in Fig. 3(a). As mentioned in Sec.II B, x_t for maximum V^R increases as t_r increases. Then, we draw ρ in the same range in Fig. 3(b) for comparison. The amplitude $\rho = P_{\uparrow}^I|_{t_{\text{wait}} \rightarrow 0}$ is obtained by fitting the experimental data of the

spin relaxation process with an exponential expression $P_{\uparrow}^M = \rho \cdot e^{-t/T_1} + \alpha$. V^R and ρ are consistent in the images with scaled colors.

To analyze this consistency, we focus on the detail of Eq.1. As shown in Fig. 3(c), we note the spin-up probability at the beginning of the readout phase as the prepared probability P_{\uparrow}^I . Throughout the STC conversion, the probability of the tunneling events detected within t_r ($P(t)$) depends on the condition probability that electron in $|\uparrow\rangle$ (F_{\uparrow}^{STC}) or $|\downarrow\rangle$ ($1 - F_{\downarrow}^{STC}$) tunnels out:

$$P(t) = F_{\uparrow}^{STC} P_{\uparrow}^I + (1 - F_{\downarrow}^{STC})(1 - P_{\uparrow}^I). \quad (3)$$

Similarly, by comparing x_{max} with x_t , the electron are measured with P_{\uparrow}^M throughout the electrical detection (F_{\uparrow}^E , F_{\downarrow}^E):

$$P_{\uparrow}^M = P(t)F_{\uparrow}^E + (1 - P(t))(1 - F_{\downarrow}^E). \quad (4)$$

We factorize Eq. 4 into sectors with and without P_{\uparrow}^I , and substitute Eq. 2 into Eq. 4 to obtain the expression of α : $\alpha = 1 - F_{\downarrow}$. Then, the relation between P_{\uparrow}^M , P_{\uparrow}^I and the V^R can be obtained by substituting Eq. 1 into Eq. 4:

$$P_{\uparrow}^M = P_{\uparrow}^I \times V^R + \alpha. \quad (5)$$

Eq. 5 reveals that P_{\uparrow}^M linearly depends on V^R . Here, the slope is P_{\uparrow}^I and the intercept is the darkcount. Since P_{\uparrow}^I only depends on the "Wait" process, we can describe the developing threshold-independent data process methods in Sec.II D.

D. Threshold-independent data process

Here, we give two threshold-independent approaches. First, we calculate the expected probability (P_{\uparrow}^E) for each t_r and x_t by applying Eq. 5 directly:

$$P_{\uparrow}^E = (P_{\uparrow}^M - \alpha)/V^R. \quad (6)$$

We define the area where $|P_{\uparrow}^E/P_{\uparrow}^I - 1| < 1\%$ as A_{eff} to represent the efficiency of the data process method, as shown in Fig. 4(a). The region inside the green dashed curves is A_{eff} , and we use the solid curves to mark A_{eff} of $|P_{\uparrow}^M/P_{\uparrow}^I - 1| < 1\%$ for comparison. P_{\uparrow}^M is obtained through the threshold-dependent method. A_{eff} of the threshold-independent method is 60 times larger than the threshold-dependent method, which means that the threshold-independent method is more robust and can calibrate the measured result from the interference of the experimental hardware limitation.

Then we try to use the linear regression to fit the P_{\uparrow}^I . By substituting Eq. 1 and $\alpha = 1 - F_{\downarrow}$ into Eq. 5, we obtain the expression of the measured probability of F_{\uparrow} and F_{\downarrow} :

$$\begin{aligned} P_{\uparrow}^M &= P_{\uparrow}^I(F_{\uparrow} + F_{\downarrow} - 1) + (1 - F_{\downarrow}) \\ &= P_{\uparrow}^I F_{\uparrow} + (P_{\uparrow}^I - 1)F_{\downarrow} + (1 - P_{\uparrow}^I). \end{aligned} \quad (7)$$

Fig. 4(b) shows the fitted result of P_{\uparrow}^I by using the standard multiple linear regression. The orange dot represents the distribution of the measured probabilities and readout fidelities

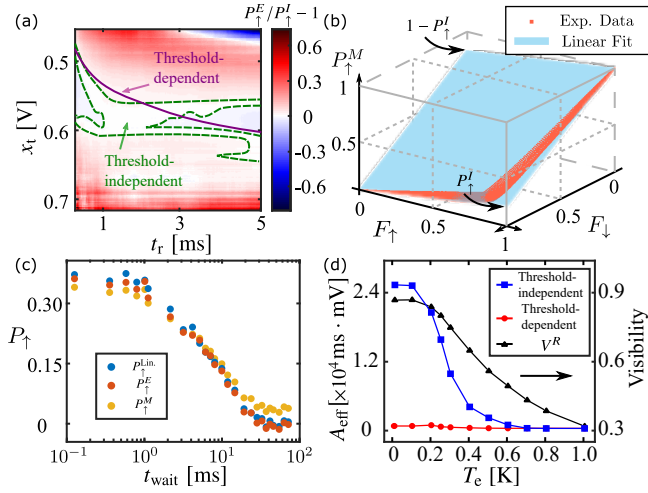


FIG. 4. (a) The bias of the expected probability (P_{\uparrow}^E) relative to P_{\uparrow}^I ($P_{\uparrow}^E/P_{\uparrow}^I - 1$) as a function of t_r and x_t . The region inside the green dashed curves indicated by "Threshold-independent" represents A_{eff} where $|P_{\uparrow}^E/P_{\uparrow}^I - 1| < 0.01$. For comparison, the purple solid curves represents A_{eff} where $|P_{\uparrow}^M/P_{\uparrow}^I - 1| < 0.01$ via the threshold-dependent method. (b) The distribution of the experiment results in $(F_{\downarrow}, F_{\uparrow}, P_{\uparrow}^M)$ space and the corresponding multiple linear regression results. The intercepts on the line parallel to the z-axis and passing $(1,0,0)$ and $(0,1,0)$ are P_{\uparrow}^I and $1 - P_{\uparrow}^I$, respectively. (c) P_{\uparrow}^E and $P_{\uparrow}^{\text{Lin}}$ are obtained from the threshold-independent methods, and P_{\uparrow}^M is obtained from the exponential decaying process. It illustrates that two threshold-independent methods suppress α and improve ρ . (d) The left y-axis shows A_{eff} as functions of T_e for the threshold-independent method and the threshold-dependent readout. And the right y-axis shows the corresponding V^R . When T_e exceeds 100 mK, V^R and A_{eff} of the threshold-independent methods decreases as T_e increases. A_{eff} of the threshold-independent method is higher than the threshold-dependent method until $T_e = 0.7$ K, where $V^R = 0.5$.

$(F_{\downarrow}, F_{\uparrow}, P_{\uparrow}^M)$, and the blue plane shows the result of the multiple linear regression. P_{\uparrow}^I can be obtained from the slope and the intercept of the plane.

By applying these threshold-independent methods directly to the experimental data and fitting the spin relaxation process of the excited spin state, Fig. 4(c) demonstrates that these two new techniques successfully suppress α and increase ρ simultaneously.

E. Influence of the Electron Temperature

Finally, we move to the influence of T_e . Ref. [30] assumed that the tunneling rate follows a Fermi distribution offset by the energy separation (ε):

$$\begin{aligned} \Gamma_{\uparrow, \downarrow}^{\text{out}} &= [1 - f(\varepsilon \pm E_z/2, T_e)] \Gamma^{\text{out}}, \\ \Gamma_{\uparrow, \downarrow}^{\text{in}} &= f(\varepsilon \pm E_z/2, T_e) \Gamma^{\text{in}}, \end{aligned} \quad (8)$$

where $f(\varepsilon \pm E_z/2, T_e)$ is the Fermi-Dirac function with $-$ for $|\downarrow\rangle$ and $+$ for $|\uparrow\rangle$, Γ^{out} (Γ^{in}) is the maximum tunnel out(in) rate, and $\Gamma_{\uparrow, \downarrow}^{\text{out}}$ ($\Gamma_{\uparrow, \downarrow}^{\text{in}}$) are tunneling rates for each spin state.

By defining $R_G = \Gamma_{\uparrow}^{\text{out}}/\Gamma_{\downarrow}^{\text{out}}$, ε can be obtained as follows:

$$\varepsilon = -k_B T_e \ln \left(\frac{1 - R_G}{R_G} \frac{1}{e^{-\frac{E_z}{2k_B T_e}} - e^{\frac{E_z}{2k_B T_e}}} \right). \quad (9)$$

We obtain the maximum tunneling rate $\Gamma^{\text{out}} = \Gamma_{\uparrow}^{\text{out}} / (1 - f(\varepsilon + E_z/2, T_e))$ and $\Gamma^{\text{in}} = \Gamma_{\downarrow}^{\text{in}} / f(\varepsilon - E_z/2, T_e)$ by substituting Eq. 8 into Eq. 9.

Then, we try to simulate the single-shot readout process for different T_e . Assuming that Γ^{out} and Γ^{in} are not associated with T_e , we directly substitute T_e into Eq. 8 to calculate the tunneling rates. We use the Monte-Carlo method to generate the simulated traces with a fixed $B_{\text{ext}} = 1.5$ T for different T_e . The left y-axis in Fig. 4(d) shows A_{eff} of the threshold-independent method and the threshold-dependent method at different T_e . The right y-axis shows the corresponding V^R . The simulation results show that A_{eff} of the threshold-independent methods is 60 times greater than the threshold-dependent method when $T_e < 0.1$ K. As T_e increases, A_{eff} of the threshold-independent methods decreases. And it is larger than the threshold-dependent method until $T_e = 0.7$ K. When $T_e > 0.7$, the corresponding $V^R < 0.5$. Here, we give the boundary condition of the threshold-independent method as $T_e = 0.7$ K when $B_{\text{ext}} = 1.5$.

III. CONCLUSION

We describe a threshold-independent method for the single-shot readout data process based on the linear dependence of P_{\uparrow}^M with the corresponding V^R and α . The fitted amplitude of the spin relaxation processes verified this relation. V^R for different t_r and x_t also reveal that the optimum readout time and threshold voltages for the single-shot readout are interrelated and should be considered simultaneously. Then, we use A_{eff} to compare the efficiency of the threshold-independent method and the threshold-dependent readout. The result shows that A_{eff} of the threshold-independent method is more than 60 times larger. Moreover, we simulate the single-shot readout process at different T_e . We broaden the boundary condition of the single-shot readout to 0.7 K with $B_{\text{ext}} = 1.5$ T, where $V^R = 0.5$. The threshold-independent method will be increasingly important as the experiment progresses to the fault tolerance threshold of the logic qubit at high electron temperature [36–38].

ACKNOWLEDGMENTS

This work was supported by the National Natural Science Foundation of China (Grants No. 12074368, 92165207, 12034018 and 61922074), the Anhui Province Natural Science Foundation (Grants No. 2108085J03), the USTC Tang Scholarship, and this work was partially carried out at the USTC Center for Micro and Nanoscale Research and Fabrication.

Appendix A: Simulation of the single-shot readout process

We use three steps to fit the parameters of the single-shot readout traces, as shown in Fig. 5(a). First, the mean value of the traces of the occupied (ionized) QD, μ_1 (μ_2), can be obtained by fitting the distribution of all data in the readout phase of x with the Gaussian Mixture Model (GMM) method as shown in Fig. 5(b). Then, we normalize the averaged readout traces (\bar{x}) by μ_1 and μ_2 , and fit $\Gamma^{\text{in,out}}$ by using the rate equations as shown in Fig. 5(c). Finally, with the knowledge of $\Gamma^{\text{in,out}}$ and $\mu_{1,2}$, we generate the simulated readout traces without noises via the Monte-Carlo method. After adding the noise to the simulated traces, we fit the standard deviations (σ_1 , σ_2) from the distribution of x_{max} in Fig. 5(d). Since the Monte-Carlo method is used only once to generate the traces, it reduces the running time of the fitting process while ensuring accuracy.

Appendix B: The STC Visibility

We employed a rate equation model to determine the expectation value of the number of electrons on QD [31]. The probabilities of the electron in three states are contained in the vector $\mathbf{P} = (P_{\uparrow}, P_{\downarrow}, P_0)$. The rate equation $d\mathbf{P}/dt = \mathbf{Q}\mathbf{P}$ describe the evolution of \mathbf{P} in time. Here, \mathbf{Q} is the transition

matrix with $\Gamma_{\uparrow}^{\text{in}}$ neglected:

$$\mathbf{Q} = \begin{pmatrix} -W - \Gamma_{\uparrow}^{\text{out}} & 0 & 0 \\ W & -\Gamma_{\uparrow}^{\text{out}} & \Gamma_{\downarrow}^{\text{in}} \\ \Gamma_{\uparrow}^{\text{out}} & \Gamma_{\downarrow}^{\text{out}} & -\Gamma_{\downarrow}^{\text{in}} \end{pmatrix} \quad (\text{B1})$$

We assume the electron is injected into QD in the "Load & Wait" phase, so we get $\mathbf{P}(0) = (P_{\uparrow}^i, 1 - P_{\uparrow}^i, 0)$. By solving the rate equation, the average trace $\bar{x}(t)$ over many periods of pulse sequences reads [32]:

$$P_0(t) = (\Gamma_{\downarrow}^{\text{out}} / \Gamma_{\downarrow}^{\text{total}}) (1 - e^{-t\Gamma_{\downarrow}^{\text{total}}}) + P_{\uparrow}^i (\Gamma_{\uparrow}^{\text{out}} - \Gamma_{\downarrow}^{\text{out}}) / (W + \Gamma_{\uparrow}^{\text{out}} - \Gamma_{\downarrow}^{\text{total}}) \times (e^{-t\Gamma_{\downarrow}^{\text{total}}} - e^{-t(W + \Gamma_{\uparrow}^{\text{out}})}), \quad (\text{B2})$$

where $P_0(t) = (\bar{x}(t) - \mu_1) / (\mu_2 - \mu_1)$ is the normalized averaged readout traces by μ_1 and μ_2 . P_{\uparrow}^i is the probability of a spin-up electron occupying QD at the beginning of the readout phase, $\Gamma_{\uparrow}^{\text{out}} (\Gamma_{\downarrow}^{\text{out}})$ is the unloading rate for electron spin up (down), $\Gamma_{\downarrow}^{\text{in}}$ is the loading rate for electron spin down, and $\Gamma_{\downarrow}^{\text{total}} = \Gamma_{\downarrow}^{\text{out}} + \Gamma_{\downarrow}^{\text{in}}$. We ignore the spin relaxation rate $W = 1/T_1$ while fitting because $\Gamma_{\uparrow}^{\text{out}} \gg W$ here. Fig. 5(c) shows the fitting results of P_0 as a function of readout time.

With the tunneling rates fitted, Ref. [27, 30] employed the method to calculate the corresponding STC conversion fidelities ($F_{\downarrow}^{\text{STC}}(t)$, $F_{\uparrow}^{\text{STC}}(t)$) and $V^{\text{STC}}(t)$ as a function of t_{r} :

$$F_{\downarrow}^{\text{STC}}(t) = e^{-t\Gamma_{\downarrow}^{\text{out}}}, \\ F_{\uparrow}^{\text{STC}}(t) = 1 - \frac{W e^{-t\Gamma_{\downarrow}^{\text{out}}} + (\Gamma_{\uparrow}^{\text{out}} - \Gamma_{\downarrow}^{\text{out}}) e^{-t(W + \Gamma_{\uparrow}^{\text{out}})}}{W + \Gamma_{\uparrow}^{\text{out}} - \Gamma_{\downarrow}^{\text{out}}}, \\ V^{\text{STC}}(t) = F_{\downarrow}^{\text{STC}}(t) + F_{\uparrow}^{\text{STC}}(t) - 1 \\ = \frac{\Gamma_{\uparrow}^{\text{out}} - \Gamma_{\downarrow}^{\text{out}}}{W + \Gamma_{\uparrow}^{\text{out}} - \Gamma_{\downarrow}^{\text{out}}} (e^{-t\Gamma_{\downarrow}^{\text{out}}} - e^{-t(W + \Gamma_{\uparrow}^{\text{out}})}). \quad (\text{B3})$$

And the corresponding $t_{\text{opt}}^{\text{STC}}$ is the following:

$$t_{\text{opt}}^{\text{STC}} = \frac{1}{W + \Gamma_{\uparrow}^{\text{out}} - \Gamma_{\downarrow}^{\text{out}}} \ln \left(\frac{W + \Gamma_{\uparrow}^{\text{out}}}{\Gamma_{\downarrow}^{\text{out}}} \right). \quad (\text{B4})$$

Appendix C: The Electrical Detection Visibility

Several methods have been used to extract V_E , including the analytical expression of the distribution [18, 19], statistic techniques [20–22], and the simulation of the readout traces [23]. Theoretically, the probability density $N_{\downarrow, \uparrow}(x)$ of x can be resolved well, as shown in Fig. 5(d), and the electrical detection fidelities can be extracted as the following:

$$F_i^E = \int_{x_s}^{x_f} N_i(x) dx, \quad (\text{C1})$$

where the integral bounds are $x_s = -\infty(x_t)$ and $x_f = x_t(+\infty)$ for $i = \downarrow(\uparrow)$, where x_t is the threshold voltage. And V^E is defined as:

$$V^E = F_{\downarrow} + F_{\uparrow} - 1. \quad (\text{C2})$$

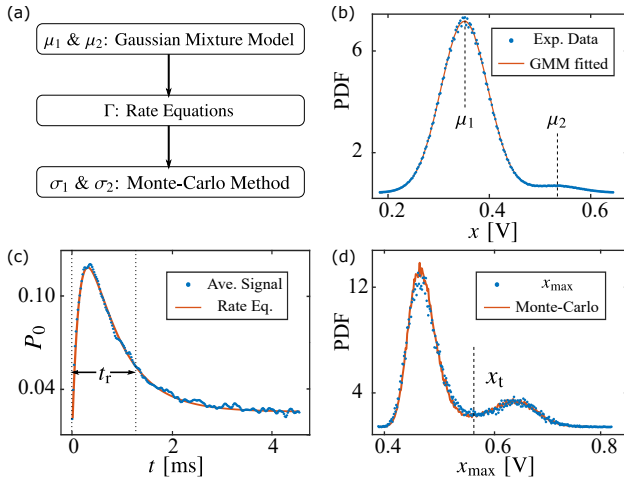


FIG. 5. (a) Three steps are applied to extract the parameters of single-shot readout process in order: (b) We use the Gaussian Mixture Model (GMM) method to fit the PDF of data in the readout phase and obtain the mean value of the traces of the occupied and ionized QD μ_1 and μ_2 . Fig. 1(c) in the main text shows two typical readout traces among all 1000 repeated measurements; (c) $\Gamma^{\text{in,out}}$ are fitted from \bar{x} via the rate equations. \bar{x} is normalized by μ_1 and μ_2 ; (d) We generate the simulated readout traces without noise via the Monte-Carlo method by using μ_1 , μ_2 and $\Gamma^{\text{in,out}}$. The standard deviations of the readout traces (σ_1 , σ_2) are fitted from the PDF of x_{max} . The dash line represent a typical position of x_t .

The numerical solution of $dV^E/dx = 0$ gives the optimum x_t where $N_{\downarrow}(x_{\text{opt}}) = N_{\uparrow}(x_{\text{opt}})$. However, it's difficult to extract

V^E directly in practice because of the lack of a simple analytical expression about the distribution of x_{max} [19].

-
- [1] J. T. Muhonen, J. P. Dehollain, A. Laucht, *et al.*, Storing quantum information for 30 seconds in a nanoelectronic device, *Nature Nanotechnology* **9**, 986 (2014).
- [2] X. Zhang, H.-O. Li, G. Cao, *et al.*, Semiconductor quantum computation, *National Science Review* **6**, 32 (2019).
- [3] J. P. Dodson, N. Holman, B. Thorgrimsson, *et al.*, Fabrication process and failure analysis for robust quantum dots in silicon, *Nanotechnology* **31**, 505001 (2020).
- [4] R. Li, L. Petit, D. P. Franke, *et al.*, A crossbar network for silicon quantum dot qubits, *Science Advances* **4**, eaar3960 (2018).
- [5] L. C. Camenzind, S. Geyer, A. Fuhrer, *et al.*, A spin qubit in a fin field-effect transistor, *arXiv preprint* **2103**, 07369 (2021).
- [6] A. M. J. Zwerver, T. Krähenmann, T. F. Watson, *et al.*, Qubits made by advanced semiconductor manufacturing, *Nature Electronics* **5**, 184 (2022).
- [7] J. Yoneda, K. Takeda, T. Otsuka, *et al.*, A quantum-dot spin qubit with coherence limited by charge noise and fidelity higher than 99.9%, *Nature Nanotechnology* **13**, 102 (2018).
- [8] K. W. Chan, W. Huang, C. H. Yang, *et al.*, Assessment of a silicon quantum dot spin qubit environment via noise spectroscopy, *Phys. Rev. Applied* **10**, 044017 (2018).
- [9] X. Xue, M. Russ, N. Samkharadze, *et al.*, Quantum logic with spin qubits crossing the surface code threshold, *Nature* **601**, 343 (2022).
- [10] A. Noiri, K. Takeda, T. Nakajima, *et al.*, Fast universal quantum gate above the fault-tolerance threshold in silicon, *Nature* **601**, 338 (2022).
- [11] A. R. Mills, C. R. Guinn, M. J. Gullans, *et al.*, Two-qubit silicon quantum processor with operation fidelity exceeding 99%, *Science Advances* **8**, eabn5130 (2022).
- [12] J. Elzerman, R. Hanson, L. W. van Beveren, *et al.*, Single-shot read-out of an individual electron spin in a quantum dot, *Nature* **430**, 431 (2004).
- [13] K. D. Petersson, C. G. Smith, D. Anderson, *et al.*, Charge and spin state readout of a double quantum dot coupled to a resonator, *Nano Letters* **10**, 2789 (2010).
- [14] P. Pakkiam, A. V. Timofeev, M. G. House, *et al.*, Single-shot single-gate rf spin readout in silicon, *Phys. Rev. X* **8**, 041032 (2018).
- [15] A. West, B. Hensen, A. Jouan, *et al.*, Gate-based single-shot readout of spins in silicon, *Nature Nanotechnology* **14**, 437 (2019).
- [16] G. Zheng, N. Samkharadze, M. L. Noordam, *et al.*, Rapid gate-based spin read-out in silicon using an on-chip resonator, *Nature Nanotechnology* **14**, 742 (2019).
- [17] J. R. Prance, B. J. V. Bael, C. B. Simmons, *et al.*, Identifying single electron charge sensor events using wavelet edge detection, *Nanotechnology* **26**, 215201 (2015).
- [18] K. C. Nowack, M. Shafiei, M. Laforest, *et al.*, Single-shot correlations and two-qubit gate of solid-state spins, *Science* **333**, 1269 (2011).
- [19] B. D'Anjou and W. A. Coish, Optimal post-processing for a generic single-shot qubit readout, *Phys. Rev. A* **89**, 012313 (2014).
- [20] D. A. Bagrets and Y. V. Nazarov, Full counting statistics of charge transfer in coulomb blockade systems, *Phys. Rev. B* **67**, 085316 (2003).
- [21] L. D. Contreras-Pulido, M. Bruderer, S. F. Huelga, and M. B. Plenio, Dephasing-assisted transport in linear triple quantum dots, *New Journal of Physics* **16**, 113061 (2014).
- [22] S. K. Gorman, Y. He, M. G. House, *et al.*, Tunneling statistics for analysis of spin-readout fidelity, *Phys. Rev. Applied* **8**, 034019 (2017).
- [23] A. Morello, J. J. Pla, F. A. Zwanenburg, *et al.*, Single-shot readout of an electron spin in silicon, *Nature* **467**, 687 (2010).
- [24] M. Veldhorst, J. C. C. Hwang, C. H. Yang, *et al.*, An addressable quantum dot qubit with fault-tolerant control-fidelity, *Nature Nanotechnology* **9**, 981 (2014).
- [25] E. Kawakami, P. Scarlino, D. R. Ward, *et al.*, Electrical control of a long-lived spin qubit in a Si/SiGe quantum dot, *Nature Nanotechnology* **9**, 666 (2014).
- [26] L. Vukušić, J. Kukučka, H. Watzinger, *et al.*, Single-shot readout of hole spins in ge, *Nano Letters* **18**, 7141 (2018).
- [27] H. Büch, S. Mahapatra, R. Rahman, *et al.*, Spin readout and addressability of phosphorus-donor clusters in silicon, *Nature Communications* **4**, 2017 (2013).
- [28] L. Robledo, L. Childress, H. Bernien, *et al.*, High-fidelity projective read-out of a solid-state spin quantum register, *Nature* **477**, 574 (2011).
- [29] A. R. Mills, C. R. Guinn, M. M. Feldman, *et al.*, High fidelity state preparation, quantum control, and readout of an isotopically enriched silicon spin qubit, *arXiv preprint* **2204**, 09551 (2022).
- [30] D. Keith, S. Gorman, L. Kranz, *et al.*, Benchmarking high fidelity single-shot readout of semiconductor qubits, *New Journal of Physics* **21**, 063011 (2019).
- [31] M. Xiao, M. House, and H. W. Jiang, Measurement of the spin relaxation time of single electrons in a silicon metal-oxide-semiconductor-based quantum dot, *Phys. Rev. Lett.* **104**, 096801 (2010).
- [32] L. A. Tracy, T. M. Lu, N. C. Bishop, *et al.*, Electron spin lifetime of a single antimony donor in silicon, *Applied Physics Letters* **103**, 143115 (2013).
- [33] M. G. House, M. Xiao, G. Guo, *et al.*, Detection and measurement of spin-dependent dynamics in random telegraph signals, *Phys. Rev. Lett.* **111**, 126803 (2013).
- [34] X. Zhang, R.-Z. Hu, H.-O. Li, *et al.*, Giant anisotropy of spin relaxation and spin-valley mixing in a silicon quantum dot, *Phys. Rev. Lett.* **124**, 257701 (2020).
- [35] R.-Z. Hu, R.-L. Ma, M. Ni, *et al.*, An operation guide of Si-MOS quantum dots for spin qubits, *Nanomaterials* **11**, 2486 (2021).
- [36] W. Huang, C. H. Yang, K. W. Chan, *et al.*, Fidelity benchmarks for two-qubit gates in silicon, *Nature* **569**, 532 (2019).
- [37] L. Petit, H. G. J. Eenink, M. Russ, *et al.*, Universal quantum logic in hot silicon qubits, *Nature* **580**, 355 (2020).
- [38] K. Takeda, A. Noiri, T. Nakajima, *et al.*, Quantum tomography of an entangled three-qubit state in silicon, *Nature Nanotechnology* **16**, 965 (2021).